INL/EXT-14-33190

Multi-scale modeling of microstructure dependent inter-granular fracture in UO2 using a phase-field based method

Pritam Chakraborty, Yongfeng Zhang, Michael R. Tonks

October 2014

The INL is a U.S. Department of Energy National Laboratory
operated by Battelle Energy Alliance

INL/EXT-14-33190

Multi-scale modeling of microstructure dependent intergranular fracture in UO2 using a phase-field based method

Pritam Chakraborty, Yongfeng Zhang, Michael R. Tonks

October 2014

Idaho National Laboratory

Idaho Falls, Idaho 83415

http://www.inl.gov

Prepared for the
U.S. Department of Energy
Office of Nuclear Energy
Under DOE Idaho Operations Office
Contract DE-AC07-05ID14517

Multi-scale modeling of microstructure dependent intergranular fracture in UO_2 using a phase-field based method

Pritam Chakraborty*, Yongfeng Zhang, Michael R. Tonks

Fuel Modeling and Simulation Department, Idaho National Laboratory (INL), Idaho Falls, ID 83401, USA

Abstract

The brittle fracture behavior of UO_2 fuels is strongly influenced by the porosity and grain size distributions in the underlying microstructure. In service, there is significant evolution of these microstructural features, which can alter the fracture properties and subsequently the thermo-physical-mechanical behavior of the nuclear fuels. To incorporate these microstructural effects on the fracture behavior, a multi-scale modeling framework is developed in the present work. Within this framework, the grain-boundary fracture properties obtained from molecular dynamics simulations are utilized in a phase-field model to investigate the intergranular brittle crack propagation in this material. A sensitivity study with varying porosity, pore and grain size is performed to investigate their influence on the fracture properties. Subsequently, the parameters of an engineering scale fracture model are obtained by fitting the stress-strain evolution obtained from the phase-field simulations. This framework provides a hierarchical coupling of properties evaluated at the atomistic scale to perform more realistic engineering level predictions of fracture in nuclear fuel pellets.

1. Introduction

The UO_2 fuel pellets undergo extensive microcracking and fragmentation during service, which strongly affects the pellet-cladding interactions,

*Corresponding author

Email address: pritam.chakraborty@inl.gov (Pritam Chakraborty)

fission gas release and consequently nuclear reactor performance. Experimental studies reveal that the pore and grain size distributions in the underlying microstructure have a strong influence on the fracture properties of the UO_2 fuels. During operation, the inhomogeneous evolution of these microstructural features causes significant spatial variation of fracture properties in the pellets and can alter the thermo-physical-mechanical behavior of the UO_2 fuel pellets. Hence, for accurate prediction of nuclear fuel performance, the development of microstructure-driven fracture models of UO_2 fuels is necessary.

The experimental studies investigating the effect of microstructure on the fracture mechanisms and properties of UO_2 fuel pellets are performed on as-manufactured sintered specimens. In [1], the brittle to ductile transition of fracture behavior with temperature has been investigated using three-point bend tests. Brittle fracture with substantial intergranular cracking has been observed below 800^oC. An increase in the proportion of transgranular fracture with lower fracture strength has also been detected for larger average grain sizes. As the temperature is increased, a transition to ductile fracture with significant plastic deformation is observed. Though this work provides an insight into the possible failure mechanisms, quantitative relations between the strength and the microstructural features, such as porosity, pore and grain size, have not been obtained. A similar study has been performed in [2] using four-point bend tests where the effect of strain rate on the fracture strength has been considered in addition to the temperature variations. It is concluded that large porosity regions in the microstructure has a stronger influence on the fracture strength than the grain size. Analytical relations between the properties like fracture strength, elasticity modulus and microstructural features such as porosity, grain size, and stoichiometry have been obtained in [3–6] using bending experiments. Additionally, the effect of the pore size on fracture strength has been quantified in [5, 6]. Compressive [7] and indentation [8–10] tests have also been performed on UO_2 fuel pellets to obtain similar relationships.

The fracture modeling of UO_2 fuel pellets have primarily focused on thermo-mechanical fragmentation process during power cycles. Numerical techniques like discrete element method (DEM) [11], or finite element method (FEM) with cohesive zone [12] or smeared crack models [13, 14] have been employed in these investigations. In DEM [11], the fracture properties are randomly distributed in the pellet to obtain the fragmentation behavior. However, the fracture properties are not correlated to the porosity, pore and

grain size distributions in the underlying microstructure. Similar correlations are missing in the fracture studies made in [12–14]. In the present work, a multi-scale method is pursued to obtain the microstructural dependent fracture parameters of a smeared crack model [14, 15] at the engineering scale. Explicit crack propagation simulations with different microstructural instantiations are performed in which the grain boundary dependent fracture properties are obtained from molecular dynamic simulations [16]. Presently, only intergranular brittle fracture has been modeled, though the same framework can be extended to capture transgranular and ductile failure mechanisms. This approach can also be utilized to obtain the irradiation dependent fracture properties as well.

To perform crack evolution in the microstructure the phase-field based fracture model proposed in [17, 18] has been utilized. Phase-field methods are widely used to model microstructure evolution [19] in which the order parameters, describing the individual phases, and their corresponding concentrations are evolved using relaxation [20] and diffusion equations [21]. The free energy that drives the evolution is constructed from the thermodynamics of the system. In the phase-field fracture models only the relaxation equation is solved to evolve the order parameter representing damage. The free energy driving the crack growth is related to the strain energy of the system. The method has been shown to capture complicated crack path [22**?** –26] and microstructure driven fracture [27–29]. Most of the available phase field fracture models are rate dependent and requires very low loading rates to capture rate independent behavior. In the model proposed in [17, 18] an artificial viscosity has been introduced which can be controlled to obtain the rate independent behavior even for large loading rates and hence used in the present work. Further, the use of a phase field approach for fracture can provide a seamless coupling to microstructure co-evolution and more accurate modeling of the thermo-physical-mechanical behavior of UO_2 fuel pellets.

The organization of the paper is as follows. In Section 2, the phase-field fracture model is introduced and sensitivity studies performed to obtain a detailed understanding of the model parameters are provided. In Section 3, the calibration of the grain boundary fracture parameters from molecular dynamic simulations is presented. In Section 4, details of the phase-field based FEM simulations to obtain porosity, pore and grain size dependent stress-strain evolution is provided. The smeared crack model and the associated parameters obtained from the phase-field based fracture simulations are described in Section 5. The paper is concluded in Section 6.

2. Phase-field based fracture model

In this work, the phase-field based fracture model proposed in [17, 18] is utilized. In this model, the order parameter, c, describing the damaged region in a 1-d scenario is represented by

$$c = \exp\left(-\frac{|x|}{l}\right) \quad \text{for} \quad -\infty < x < \infty \tag{1}$$

where l is a length parameter that controls the thickness of the damaged region and the sharp crack limit is approached as $l \to 0$. The damage variable (c) varies from 0 to 1, where 0 and 1 represents the undamaged and completely damaged states, respectively. A schematic of the damaged profile is shown in Fig. 1 where the crack front is in a direction perpendicular to the plane of the paper at x=0.

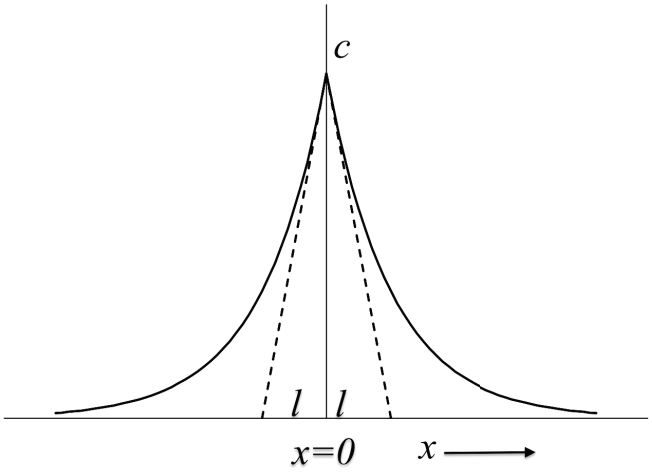

Figure 1: 1d spatial distribution of phase-field variable representing damage (c).

By using the principle of variations, the area of the damaged surface is obtained in [17, 18] as

$$\Gamma_l = \frac{1}{2l}\int_\Omega \left(c^2 + l^2\left|\nabla c\right|^2\right) d\Omega \tag{2}$$

where Ω is the volume of the domain. Under the application of an external load, the power balance equation of brittle fracture follows

$$\dot{E}_E + \dot{E}_D = P_E \tag{3}$$

where $\dot{E}_E$ is the rate of change of strain energy of the system, $\dot{E}_D$ is the dissipative power due to crack propagation and P_E is the power due to the applied load on the system. In [17, 18], the rate of change of strain energy of the system is assumed to have the form

$$\dot{E}_E = \frac{d}{dt}\int_\Omega \psi d\Omega \quad \text{where} \quad \psi = \left[(1-c)^2 + k\right]\psi_0^+ + \psi_0^- \tag{4}$$

where k is a small value that ensures the positive definiteness of the system after complete damage (c=1) and

$$\psi_0^\pm = \lambda \left\langle \epsilon_1 + \epsilon_2 + \epsilon_3 \right\rangle_\pm^2 /2 + \mu\left(\left\langle \epsilon_1 \right\rangle_\pm^2 + \left\langle \epsilon_2 \right\rangle_\pm^2 + \left\langle \epsilon_3 \right\rangle_\pm^2\right) \tag{5}$$

where ψ_0^+ and ψ_0^- are the positive and negative components of the specific strain energies, respectively. In Eq. 5, ϵ_1, ϵ_2, ϵ_3 are the principal strains, λ is the Lame's constant and μ is the shear modulus. The operators $\langle\rangle_\pm$ are defined as $\langle x\rangle_\pm = (x \pm |x|)/2$.

As can be observed from Eqs. 4 and 5, degradation due to damage in this model is only associated with positive principal strains. Under the action of compressive strains, stresses arising due to contact of cracked surfaces are considered. The stress tensor is obtained from Eqs. 4 and 5 as

$$\underline{\underline{\sigma}} = \frac{\partial \psi}{\partial \underline{\underline{\epsilon}}} = \left[(1-c)^2 + k\right]\frac{\partial \psi_0^+}{\partial \underline{\underline{\epsilon}}} + \frac{\partial \psi_0^-}{\partial \underline{\underline{\epsilon}}} = \left[(1-c)^2 + k\right]\underline{\underline{\sigma_0^+}} - \underline{\underline{\sigma_0^-}} \tag{6a}$$

$$\underline{\underline{\sigma_0^\pm}} = \sum_{a=1}^{3}\left[\lambda\left\langle \epsilon_1 + \epsilon_2 + \epsilon_3\right\rangle_\pm + 2\mu\left\langle \epsilon_a\right\rangle_\pm\right]\underline{n_a}\otimes\underline{n_a} \tag{6b}$$

where $\underline{n_a}$ are the eigen vectors of the strain tensor $\underline{\underline{\epsilon}}$.

The dissipative power in Eq. 3, is described by

$$\dot{E}_D = \int_\Omega g_c \dot{\gamma} d\Omega \tag{7}$$

where g_c is an energy release rate type parameter and

$$\gamma = c^2/2l + l\left|\nabla c\right|^2/2 \tag{8}$$

To ensue irreversibility in damage evolution, i.e.

$$\dot{\gamma}_l(c) = \int_\Omega \frac{\partial \gamma}{\partial c} \dot{c} d\Omega \geq 0 \tag{9}$$

the following has been incorporated in the model [17, 18]: (i) appropriate choice of free energy to maintain non-negative $\partial\gamma/\partial c$ and (ii) penalty type constraint on Eq. 7 to enforce $\dot{c} \geq 0$.

In [17, 18], both the rate independent and dependent versions of the fracture model, satisfying the above-stated constraints, are provided. In the present work, the rate dependent form has been chosen and involves the following coupled system of equations:

$$\nabla . \left(\left[(1-c)^2 + k \right] \underline{\underline{\sigma_0^+}} - \underline{\underline{\sigma_0^-}} \right) = 0 \tag{10a}$$

$$l \Delta c - \beta = 0 \tag{10b}$$

$$\dot{c} - \frac{1}{\eta} \left\langle \beta + 2(1-c) \frac{\psi_0^+}{g_c} - \frac{c}{l} \right\rangle_+ = 0 \tag{10c}$$

where η is a viscosity parameter. The rate independent limit can be approached as $\eta \to 0$. The weak form of the coupled system in Eq. 10 is obtained as

$$\int_\Omega \nabla \delta \underline{u} . \left(\left[(1-c)^2 + k \right] \underline{\underline{\sigma_0^+}} - \underline{\underline{\sigma_0^-}} \right) d\Omega - \int_\Gamma \delta \underline{u} . \underline{t} d\Gamma = 0 \tag{11a}$$

$$\int_\Omega \nabla \delta\beta . l \nabla c d\Omega + \int_\Omega \delta\beta \beta d\Omega - \int_\Gamma \delta\beta l \nabla c . \underline{n} d\Gamma = 0 \tag{11b}$$

$$\int_\Omega \delta c \left(\dot{c} - \frac{1}{\eta} \left\langle \beta + 2(1-c) \frac{\psi_0^+}{g_c} - \frac{c}{l} \right\rangle_+ \right) d\Omega = 0 \tag{11c}$$

where $\delta \underline{u}$, $\delta\beta$ and δc are the test functions. The weak form in Eq. 11 is implemented in INLs mesoscale MARMOT code based on the MOOSE framework [30] and numerically integrated using the backward Euler scheme.

2.1. Example 1

A 1d strain-controlled problem is considered to explore the behavior of damage evolution obtained from the rate dependent formulation. A cyclic

Table 1: The properties used to perform 1-d simulation.

E (GPa)	g_c (GPa-mm)	l (mm)	η (s/mm)	k (GPa)
210	0.001	0.01	10^{-4}	10^{-6}

strain, shown in Fig. 2(a), is applied and Eq. 10c is numerically integrated using a backward Euler scheme. A strain rate of 1 /s is used in this case. The interfacial term appearing in Eqs. 10b and 10c is ignored. The parameters used in this simulation are shown in Table 1.

The evolution of stress and damage is shown in Fig. 2(b) and 2(c), respectively. As can be observed from Fig. 2(b), elastic unloading with a damaged stiffness occurs after strain reversals and corroborates with other type of brittle fracture models. The evolution of damage tends to saturate once $c > 0.95$ and is shown in Fig. 2(c).

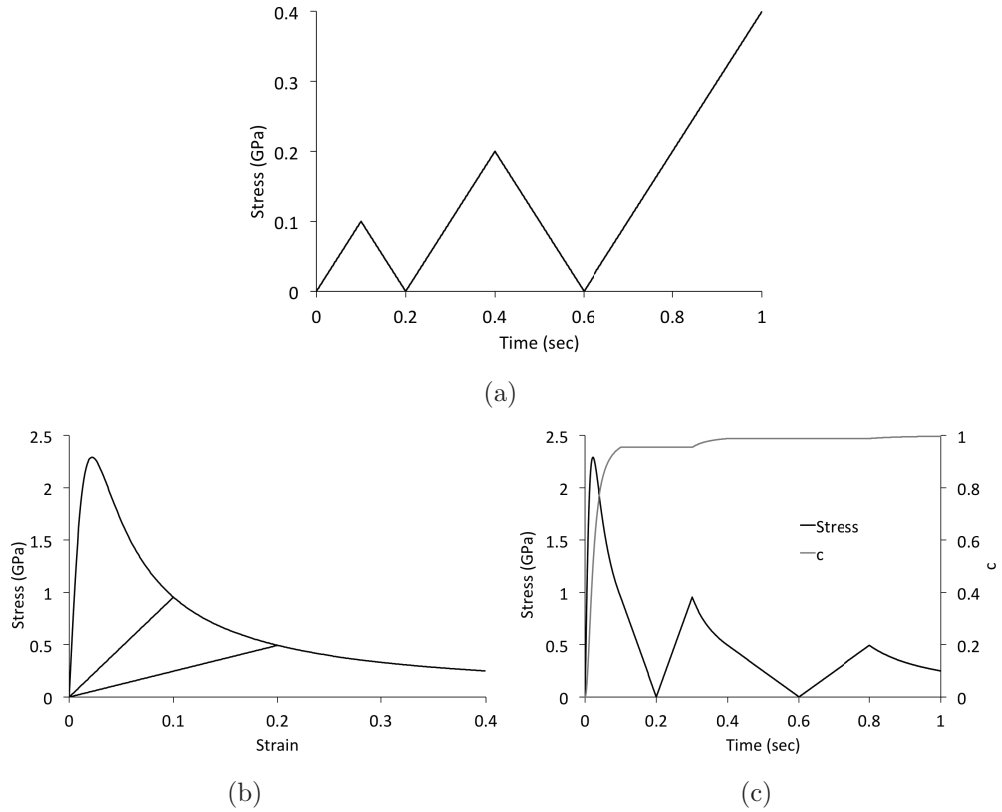

Figure 2: The evolution of stress and damage in a 1d cyclically strained problem. (a) Cyclic strain with time; (b) Stress-strain evolution; (*c*) Stress and damage evolution with time.

The influence of strain rate and η on the damage behavior is shown in Fig. 2. At higher values of η, the stress-strain evolution varies significantly with strain rate. However as $\eta \to 0$, a strain rate independent behavior can be achieved as shown in Fig. 3.

Table 2: The properties used to perform phase-field based FEM simulation of SENT specimen.

E (GPa)	ν	g_c (GPa-mm)	l (mm)	η (s/mm)	k (GPa)
207	0.3	0.0027	0.0075	10^{-4}	10^{-6}

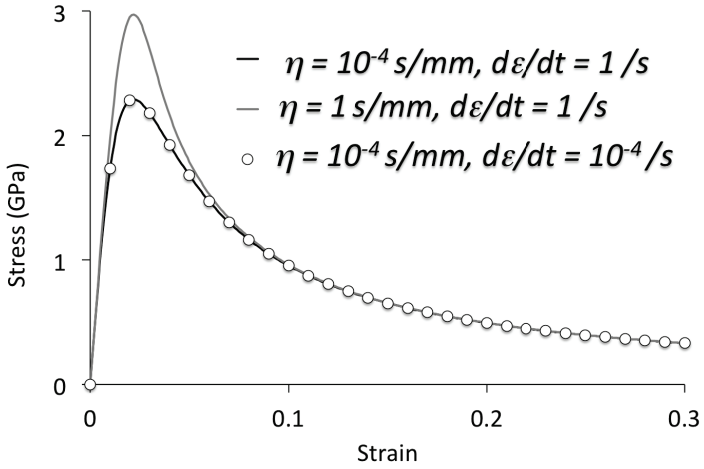

Figure 3: The effect of viscosity and strain rate on the 1d stress-strain behavior for a applied strain with constant strain rate.

2.2. Example 2

The single edge notch tension (SENT) specimen shown in Fig. 4(a) is used to demonstrate the workability of the method. The properties used to represent the rate independent sharp crack propagation are shown in Table 2.

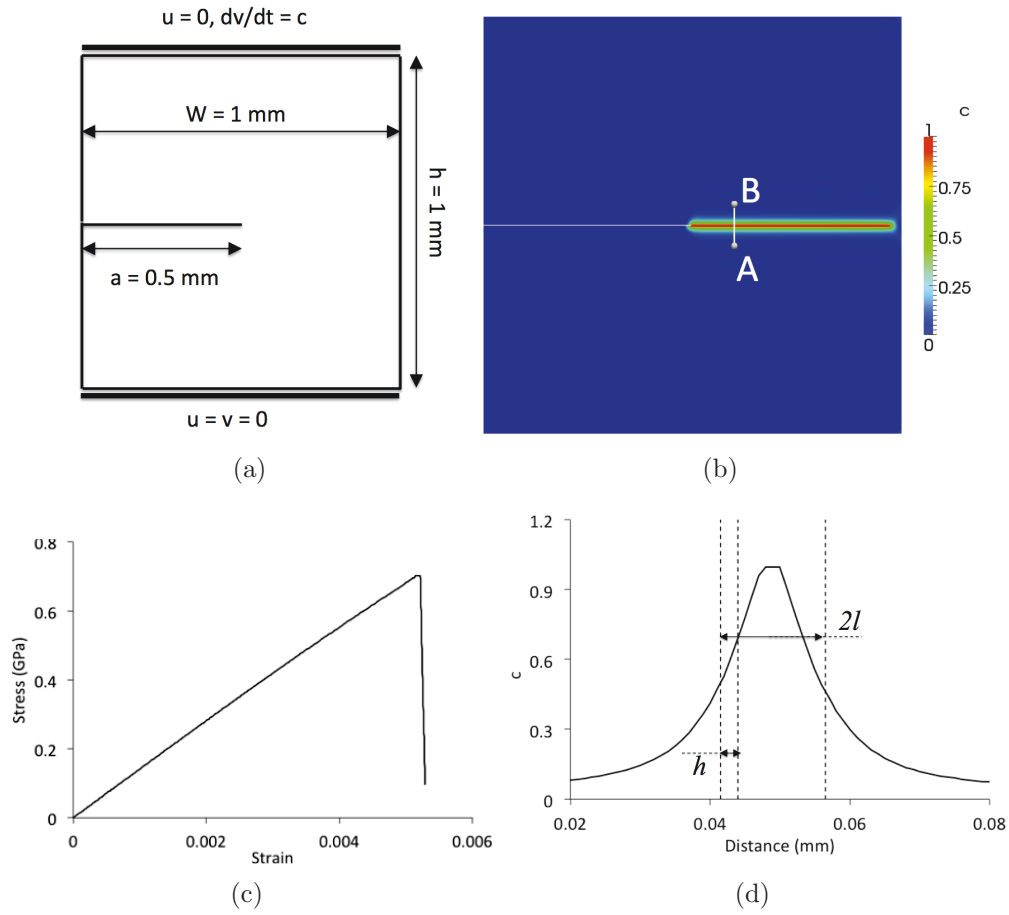

Figure 4: Simulation of brittle Mode I crack propagation in single edge notch (SENT) specimen using phase-field based fracture model: (a) Specimen geometry and boundary conditions; (b) Final configuration; (c) Stress-Strain along loading direction; (d) Variation of 'c' along a line A-B on the crack shown in (b).

Based on the length parameter (l), a uniform mesh size $h = 0.0025$ mm can provide a mesh independent solution [17, 18] and is used to discretize the FEM model. The final configuration of the specimen and the corresponding stress-strain curve is shown in Fig. 4(b) and 4(c), respectively. As can be observed from Fig. 4(c), the model is able to replicate the brittle fracture behavior, characterized by an immediate unloading beyond a critical load. The variation of the phase-field variable, c, along a line A-B on the crack (4(b)) is shown in Fig. 4(d) and a comparison between the thickness of the damaged zone and mesh size is also provided.

This example suggests that the model can capture the rate independent brittle crack propagation satisfactorily. However the response strongly depends on the mesh size (h), η and l. Hence sensitivity studies are performed in the following sub-sections to investigate these dependencies. Further, the difference between the energy release rate (G) used in linear elastic fracture mechanics and g_c is established, followed by a study to investigate the sensitivity of fracture stress and energy on g_c.

2.3. Mesh size independence of the fracture model

As stated in [17, 18], the mesh independent behavior of the model is guaranteed only when the interface is sufficiently resolved and the mesh size, h, satisfies $h < l/2$. To verify this behavior, fracture simulations of the SENT are performed using $h = 0.01$. 0.005, 0.0025 and 0.00125 mm for $l = 0.0075$ mm and $\eta = 10^{-3}$ s/mm. The stress-strain curves are compared in Fig. 5. Mesh dependency can be observed in the figure for $h > l/2$ confirming that an upper bound on h is necessary to obtain a mesh independent solution.

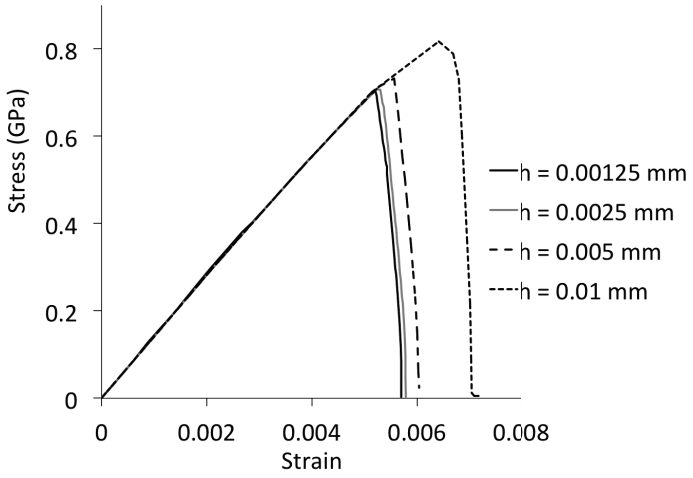

Figure 5: The effect of mesh size on the stress-strain behavior of SENT specimen. The following parameters are used: $l = 0.0075$ mm, $\eta = 10^{-3}$ s/mm.

2.4. Sensitivity of the brittle fracture behavior to the viscosity parameter

In the phase-field model, the viscosity parameter (η) is used to improve the convergence characteristics by regularizing the fracture behavior through additional dissipation. However, such artificial dissipation can have a strong

influence on the predicted fracture properties. For instance, while the use of higher η values allow larger displacement increments, it increases the fracture stress and energy values. To evaluate this influence, Mode I crack propagation in the SENT specimen described previously is simulated using different η values but the same $l = 0.0075$ mm and $g_c = 2.7$ MPa-mm. A mesh size of 0.0025 mm is used in all the simulations. The stress-strain curves are shown in Fig. 6(a). As can be observed from the figure, though higher viscosities smoothens the unloading behavior, they increase the maximum stress and dissipated energy significantly. A convergence to rate independency can be observed in Fig. 6(b) and 6(c) with decreasing viscosity. Hence, the viscosity parameter needs to be chosen judiciously to obtain computational speed-up in conjunction with the near rate independent solution.

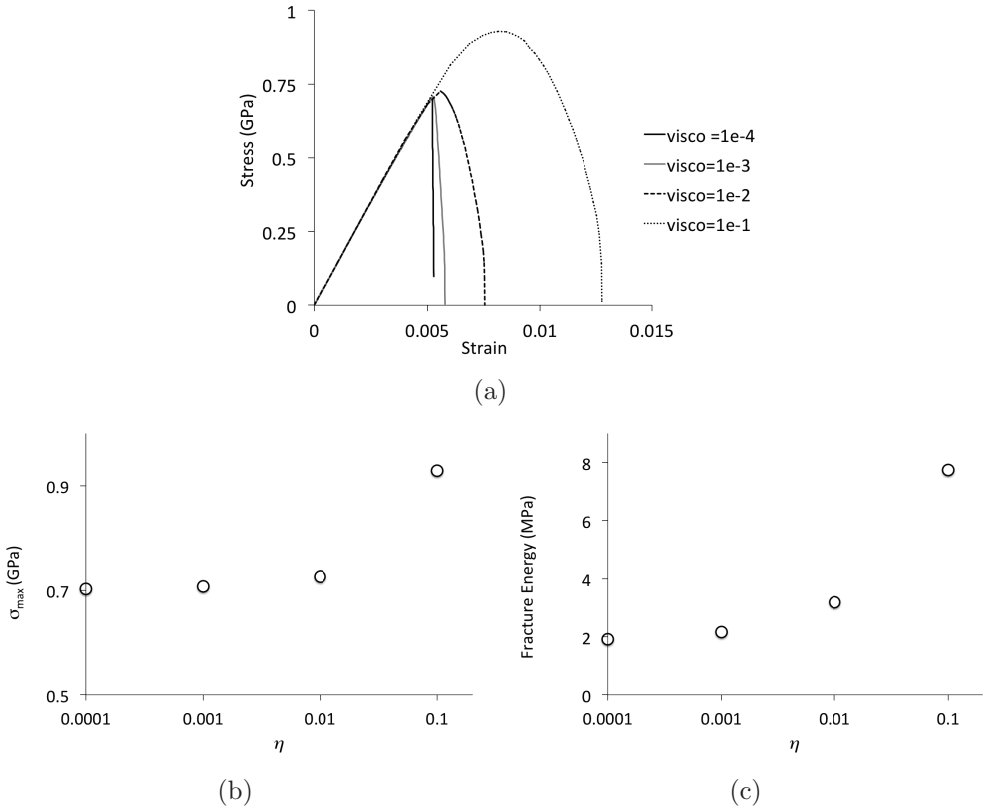

Figure 6: Sensitivity of fracture behavior on η obtained from fracture simulations of SENT specimen: (a) Stress-strain along loading direction; (b) Variation of σ_{max}; (c) Variation of fracture energy calculated from the area under the curves shown in (a).

2.5. Sensitivity of the brittle fracture behavior to the characteristic length parameter

The characteristic length parameter (l) controls the size of the damage region and tends to a sharp crack as $l \to 0$. Though the use of large l values can cause significant deviation in the fracture properties, the minimum possible size of l is determined by the size of the FEM problem and computational feasibility. Hence, investigating the influence of l on the brittle fracture behavior and properties is necessary, and is performed by simulating crack propagation in the SENT specimen using different l values but the same $\eta = 10^{-4}$ s/mm and $g_c = 1$ MPa-mm. The simulations are performed with the h -adaptivity feature in MOOSE [30] in which the maximum mesh size (h_{max}) at crack tip is controlled such that $h_{max} < l/2$. In Fig. 7, the automatic mesh adaptivity with the propagating crack is shown.

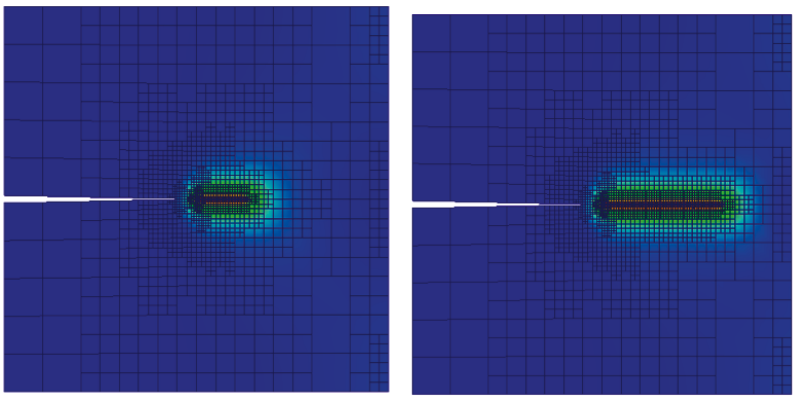

(a) (b)

Figure 7: Adaptive mesh refinement with crack propagation: (a) $\sigma = 276$ MPa, $\epsilon = 0.0033642$; (b) $\sigma = 152$ MPa, $\epsilon = 0.0033665$.

The stress-strain curves for different l values are compared in Fig. 8(a). Since, the allowable size of the diffused damage zone increases with l, the stress-strain evolution shows larger non-linearity prior to unloading for higher values of l. The maximum stress and fracture energy also reduces with increasing l as seen in Fig. 8(b) and 8(c), respectively.

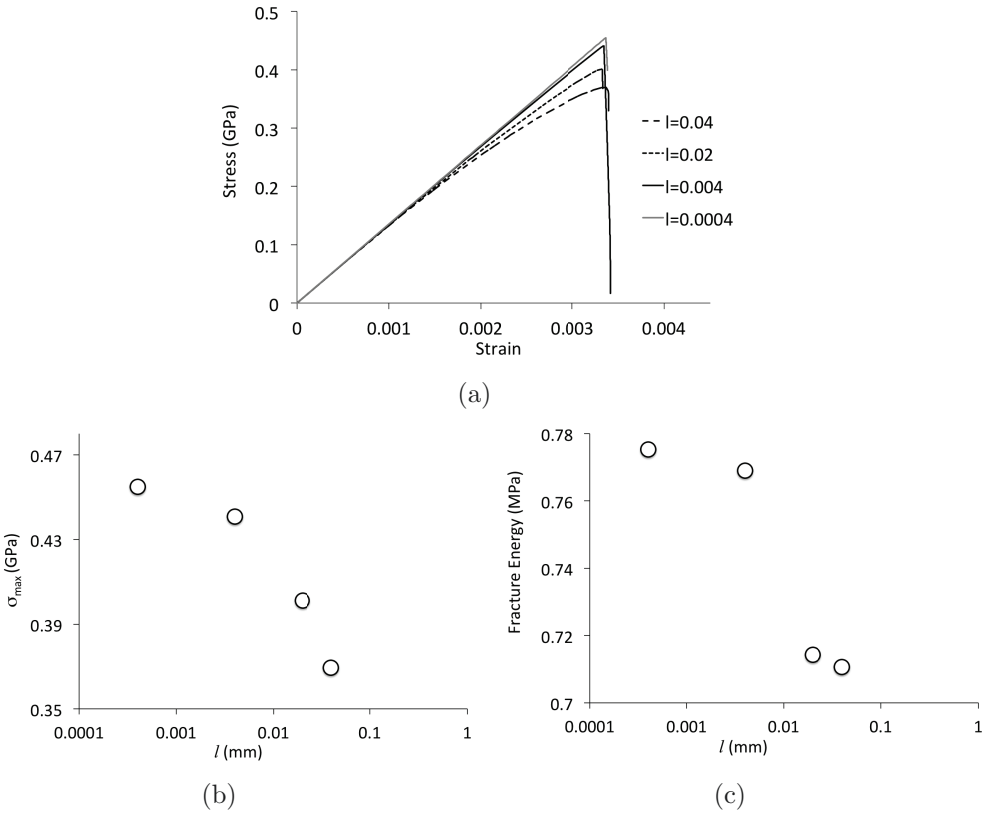

Figure 8: Sensitivity of fracture behavior on l obtained from fracture simulations of SENT specimen: (a) Stress-strain along loading direction; (b) Variation of σ_{max}; (c) Variation of fracture energy calculated from the area under the curves shown in (a).

As can be observed from the figures, saturation of the fracture stress/energy values occurs at both the extremes (small and large l) and is due to the following:

1. As the l value is continuously decreased, these values converge towards the sharp crack limit.
2. Though l sets the bound on the size of the damaged region, the amount of damage is dictated by the stress intensification caused by the defect and hence the associated defect size or crack length also plays a crucial role. Thus, beyond a certain upper limit of l, the maximum extent of damage is achieved for a given cracked geometry and subsequent increase of l has no effect on the fracture stress and energy.

2.6. The relationship between energy release rate (G) and g_c

In the phase-field based fracture model, the dissipative power is related to the crack growth rate through the parameter g_c shown in Eq. 7. This parameter is similar to the energy release rate (G) defined as

$$G = -\frac{\partial (U - W)}{\partial A} \tag{12}$$

in linear elastic fracture mechanics (LEFM), where U is the strain energy, W is the external work and A is the crack area. Crack initiation and growth is considered to happen when a critical energy release rate, G_c, which forms a fracture property, is exceeded, i.e. $G \geq G_c$. Brittle fracture is characterized by a flat G-curve ($G = G_c$) which implies that for rate independency and in the sharp crack limit, g_c should be equal to G_c.
To verify this conclusion, the Mode-I J-integral for the SENT specimen, shown in subsection 2.2, is evaluated using ABAQUS [31]. The evolution of J with applied stress is shown in Fig. 9(a). The stress at unstable failure can then be obtained based on $G_c = g_c = 2.7$ MPa-mm and is shown in Fig. 9(b). As can be observed from the figure, unstable crack propagation in the phase-field based fracture simulation occurs at a larger stress than that predicted by LEFM. Hence, experimentally obtained G_c values are not directly usable as the parameter g_c in the phase-field based fracture model and calibration is necessary.

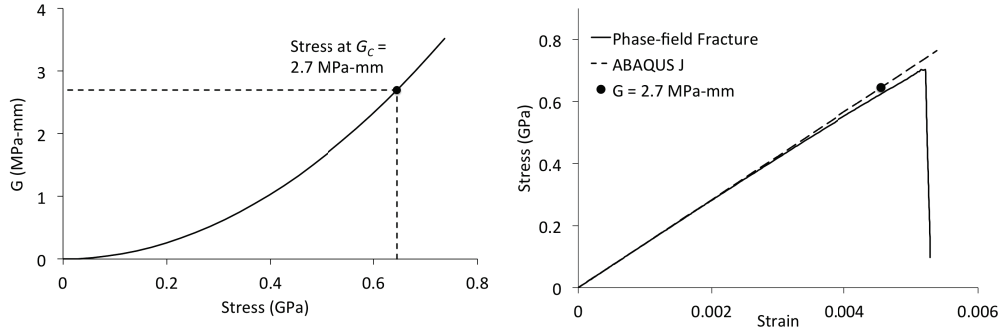

(a) (b)

Figure 9: Comparison of critical energy release rate (G_c) for brittle fracture and g_c used in phase-field based fracture model: (a) Evolution of G with stress; (b) Stress at unstable crack propagation for $G_c = 2.7$ MPa-mm and from phase-field based fracture simulation for $g_c = 2.7$ MPa-mm

2.7. Sensitivity of the brittle fracture behavior to the energy release rate type parameter g_c

Phase-field based fracture simulations of the SENT specimen is performed using 3 different g_c values, viz. 0.5, 1 and 2 MPa-mm, $l = 0.0075$ mm and $\eta = 10^{-4}$ s/mm. The stress-strain evolutions are shown in Fig. 10(a). With larger values of g_c , both the fracture stress and energy increases as can be observed from the figure. The variation of fracture stress (σ_{max}) with g_c follows: $\sigma_{max} \propto \sqrt{g_c}$, as can be observed from the fit in Fig. 10(b). This corroborates with the dependence of fracture stress on critical energy release rate, G_c, in Mode-I linear elastic brittle fracture: $K_{IC} = \sigma_{max}\sqrt{W} f(a/W) = \sqrt{G_c E}$, where K_{IC}, a, W and E are the fracture toughness, crack length, specimen width and Young's modulus, respectively. A sharp unloading in brittle crack propagation implies that the fracture energy is linearly dependent on g_c and is obtained from the fit shown in 10(c). These relationships can be utilized to calibrate g_c from stress-strain curves obtained from fracture experiments or lower length scale models by performing only two simulations once the elastic properties are known.

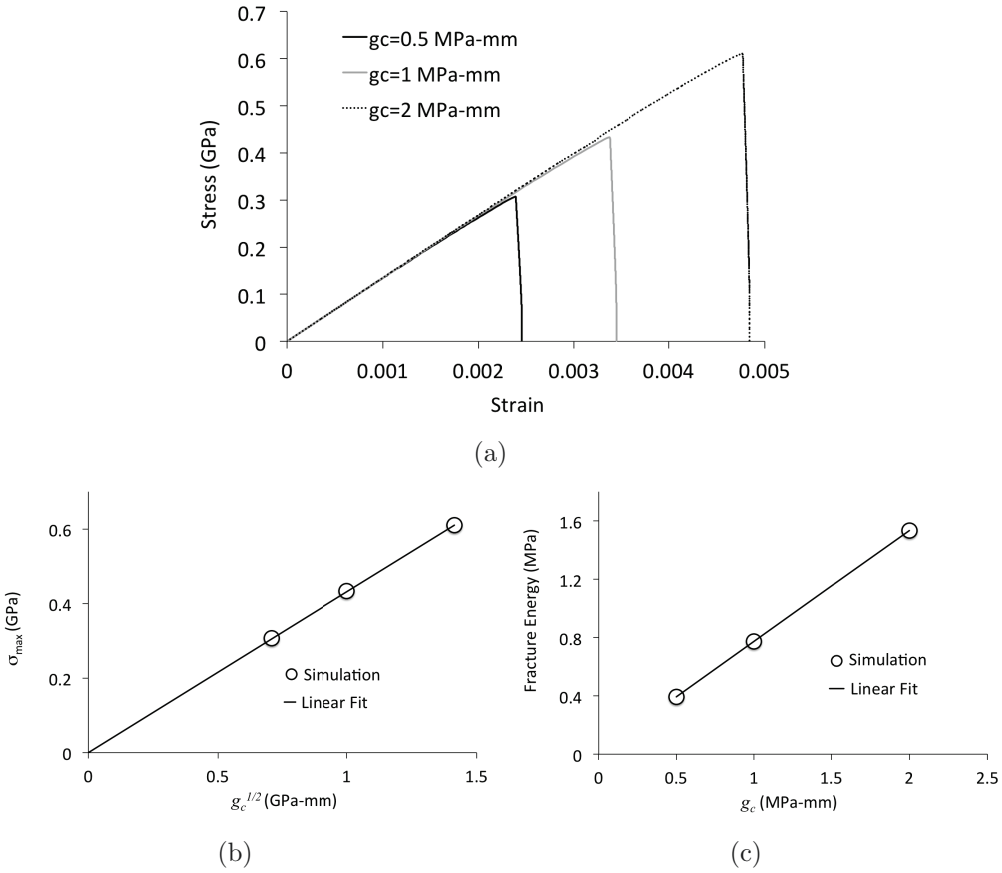

Figure 10: Sensitivity of fracture behavior on g_c obtained from fracture simulations of SENT specimen: (a) Stress-strain along loading direction; (b) Variation of σ_{max}; (c) Variation of fracture energy calculated from the area under the curves shown in (a).

3. Calibration of grain boundary fracture parameters

To perform the microstructure driven fracture simulations using phase-field based model, the g_c parameter values for different grain boundary types is required. In this work, the stress-strain behavior of the $\Sigma 3$ grain boundary obtained from molecular dynamic (MD) simulations is fitted with the phase-field based model to obtain this parameter. The details of the calibration process to obtain the fracture parameters are described below.

3.1. Molecular dynamics (MD) simulations

In the MD simulations, a sensitivity study with nine different inter-atomic potentials is performed to obtain the energy release rate for intergranular fracture in UO_2. The details of the MD simulations are provided in [16]. A schematic of the simulation set-up can be seen in Fig. 11. For the MD simulations periodic boundary conditions are applied on the x-faces, whereas for the phase-field simulations the symmetry boundary conditions shown in Fig. 11 are used. In the MD simulations, the top and the bottom halves of the simulation cell each represent a grain. The two grains are symmetrically tilted with respect to each other about the <110> axis for about 71^o, resulting in two <110> symmetrical tilt $\Sigma 3$ grain boundaries due to the periodicity, one in the middle and the other at the border (top and bottom). The system dimensions are $30.5 \times 36.0 \times 3.2$ nm, with an elliptical hole of size 8×2 nm along the grain boundary in the middle. The loading is applied by adjusting the y coordinate of each atom by 10^{-4} for every 1 ps, corresponding to a nominal engineering strain rate of 10^8/s. To evaluate the atomistic stresses, the Virial stress formulation was utilized to obtain the stress-strain curve. The nominal stress was represented by the average of the atomistic stresses over the entire volume.

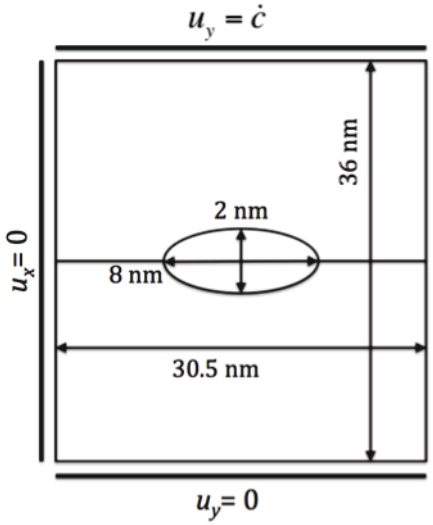

Figure 11: Schematic of the volume element consistent with MD used to calibrate the g_c parameter.

3.2. Calibration of the g_c parameter from MD simulations

A numerical sensitivity study is performed where the g_c value is modified and the stress-strain curve from plane stress FEM simulation of the volume element shown in Fig. 11 is compared with the MD results given by the Yakub potential. For the <110> symmetrical tilt $\Sigma 3$ grain boundary brittle intergranular fracture is observed, as indicated by the stress-strain curve in Fig. 12(a). Similar stress-strain curve is generated by several other potentials. In the FEM simulations, l =1 nm (as observed in the MD simulations) and $\eta = 10^{-4}$ nm/s are used. For $g_c = 0.002$ MPa-mm, a good agreement is obtained as shown in Fig. 12(a). The final configuration of the volume element is shown in Fig. 12(b). In the intergranular fracture simulations, all the grain boundaries are assumed as <110> symmetrical tilt $\Sigma 3$ and the calibrated g_c value is used.

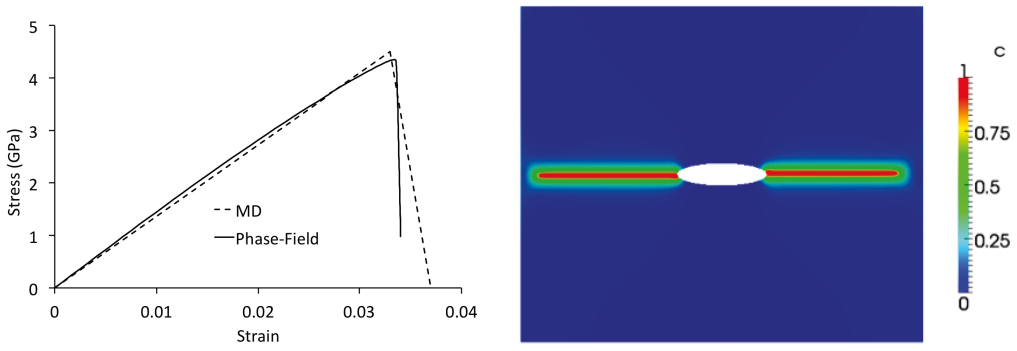

(a) (b)

Figure 12: (a) Comparison of the stress-strain evolution between the phase-field based plane stress FEM and MD simulation.(b) Final configuration of the volume element.

3.3. Transferability of the g_c parameter

The length scale of the representative volume element considered for intergranular fracture studies (40-80 μm) are much larger than the atomistic scale ($\sim$40 nm). Hence, due to the constraint on the mesh size, the minimum l parameter achievable in the intergranular fracture analyses is much larger than that used in calibration from the MD simulations (1 nm). Thus, the transferability of the g_c parameter for different l values needs to be established prior to performing the fracture analyses.

A symmetric center crack problem is thus considered using two similar geometries, but where one is hundred times larger than the other. The l parameter and mesh size is also scaled accordingly, while the g_c parameter is kept fixed. Very low viscosity values are used in both the cases to ensure near rate independent behavior. The stress-strain behavior for both the cases is shown in Fig. 13. Identical $\sigma\sqrt{W}$ can be obtained for both the geometries as seen in Fig. 13(b), which in LEFM implies that

$$K_{IC} = K_{IC-2X} \quad \text{since} \quad K = \sigma\sqrt{W} f\left(a/W\right) \tag{13}$$

where K_{IC} and K_{IC-2X} are the fracture toughnesss of the unscaled and scaled geometries, respectively. Hence, for near rate independency and sharp crack limit, the fracture toughness and energy release rate is unaltered by scaling the geometry, mesh and length scale parameter. Hence, the g_c parameter used in phase-field based fracture model is transferrable between different length scales as long as the minimum mesh size resolves the defect geometry appropriately.

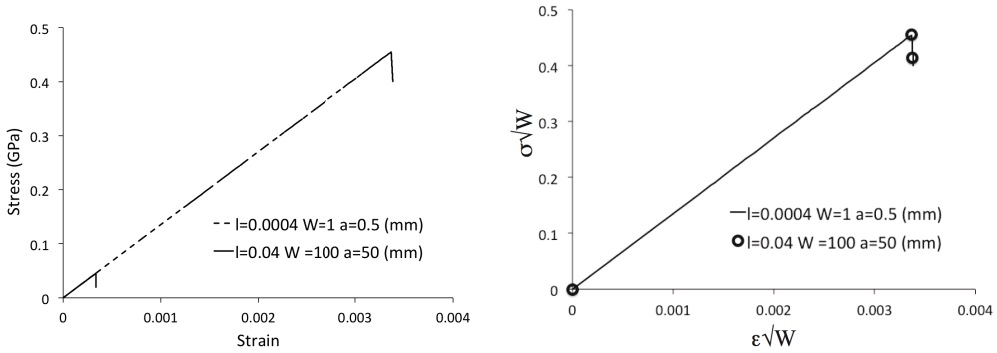

(a) (b)

Figure 13: Comparison of: (a) Stress-strain evolution, and (b) $\sigma\sqrt{W} - \epsilon\sqrt{W}$ between the un-scaled and scaled symmetric center crack geometries.

4. Phase-field based intergranular fracture simulation

A numerical sensitivity study is performed in which the porosity, pore and grain size effects on the fracture strength are investigated. An average grain size of 8 μm, which has been typically observed in experiments, is considered. The porosity is varied from 2-5% with a uniform pore diameter of

1 μm and the pores are randomly distributed on the grain boundaries. The pores act as crack initiators, and hence to spatially resolve the stress concentrations a length parameter $l = 0.1$ μm is used. To enforce intergranular crack propagation, g_c of 0.002 MPa-mm and 0.01 MPa-mm are used at the grain boundaries and interior, respectively. A uniform Young's modulus, E = 385 GPa, and Poisson's ratio, $\nu = 0.23$, typical for UO_2 [32] are used in all the simulations.

4.1. Effect of randomness of microstructure

A representative volume element of size 40 μm $\times$ 40 μm with $\sim$32 grains with average grain size of 8 μm is considered. Three different random microstructures are generated and are subjected to boundary conditions shown in Fig. 14. One of the microstructure is displaced along the y-direction rather than the x-direction as shown in Fig. 14 in order to consider any anisotropy effects due to the pore distribution in the microstructure. The fractured configuration of a microstructure and a comparison of the stress-strain evolution are shown in Fig. 15(a) and 15(b), respectively. The variations in the stress-strain evolution observed in Fig. 15(b) suggest that the size of the volume element and the number of grains are reasonable for this study.

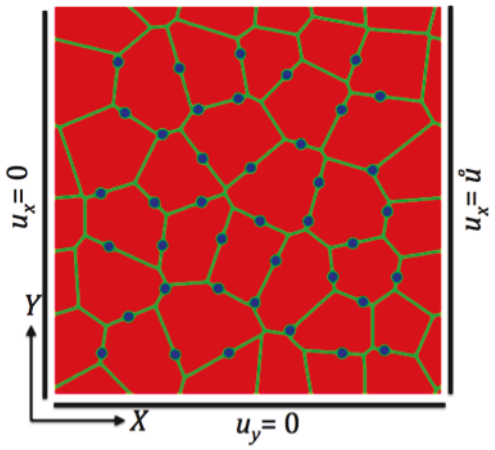

Figure 14: Random microstructure of size 40 μm $\times$ 40 μm with $\sim$32 grains of average grain size 8 μm and porosity 2% with randomly distributed pores with a uniform pore diameter of 1 μm. Symmetric boundary conditions, as shown in the figure, are used to perform the phase-field based fracture simulations.

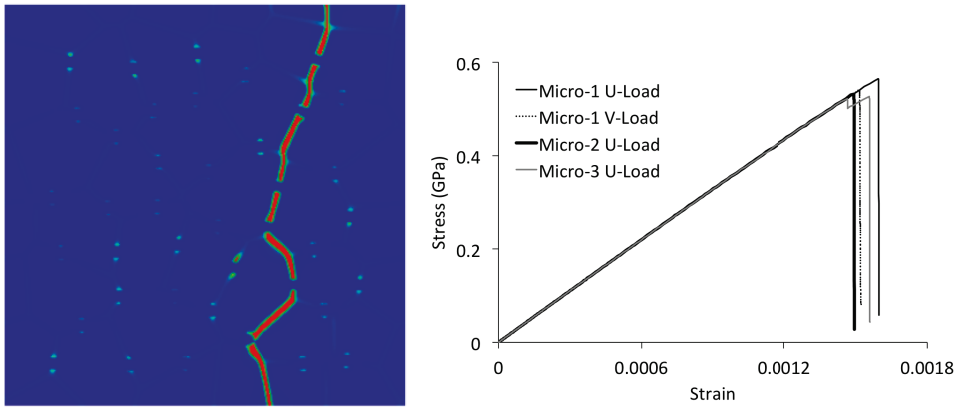

(a) (b)

Figure 15: (a) Final configuration. (b) Stress-strain evolution of random microstrcutures loaded along X or Y directions.

4.2. Effect of strain ratio

One of the microstructures is subjected to different strain ratios and the stress-strain evolution is shown in Fig. 16. The cracked configuration for $\epsilon_2/\epsilon_1 = 0$ and $\epsilon_2/\epsilon_1 = 1$ is shown in Fig. 17. A change in crack path due to a difference in strain ratio is evident.

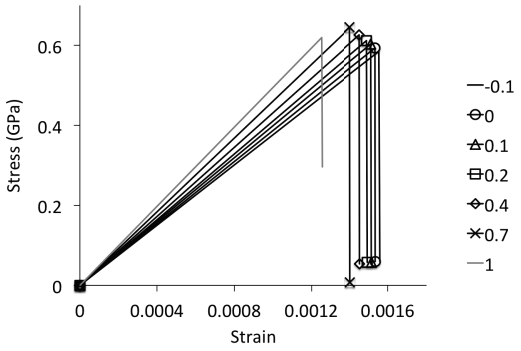

Figure 16: Comparison of stress-strain evolution along the primary loading direction for different strain ratios (ϵ_2/ϵ_1).

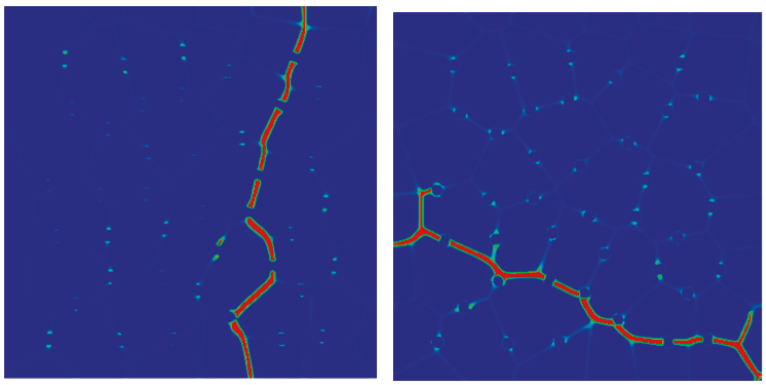

(a) (b)

Figure 17: Final configuration for different macroscopic strain ratios: (a) $\epsilon_2/\epsilon_1 = 0$ (b) $\epsilon_2/\epsilon_1 = 1$.

4.3. Effect of porosity and pore size

The porosity in one of the microstructure is increased from 2-5% and the stress-strain evolution is compared in Fig. 18. As can be observed from the figure, with increase in porosity a decrease in the effective elastic modulus and fracture stress occurs. A functional form describing this dependency is provided in the next section.

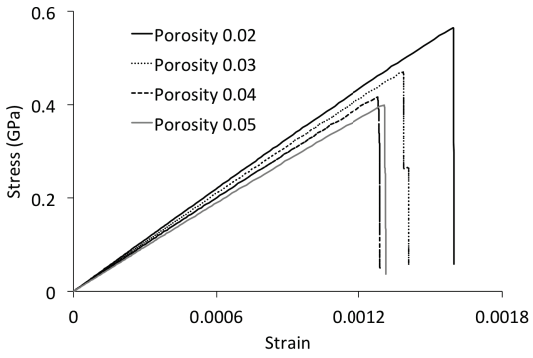

Figure 18: Comparison of stress-strain evolution along the primary loading direction for different porosities.

A higher pore size increases the stress-concentration for the same macroscopic load and hence can reduce the fracture stress. However, the alignment of a grain boundary with the loading direction, where crack initiation can

happen due to the presence of a pore, also influences the macroscopic stress to fracture. Hence, increase in pore size for the same porosity can either increase or decrease the fracture stress depending on the probability of obtaining such pore-grain boundary combinations that can cause earlier intergranular fracture. Thus the size of the representative volume element is very crucial in determing the effect of pore size on the fracture stress. In the present study, a reduced fracture stress is obtained with an increase in pore diameter (1 and 2 μm) for the same porosity of 2% and is shown in Fig. 19. For the larger pore size, the propagating crack is arrested and requires additional energy to cause further growth. The effective elastic modulus is unaffected by the pore size as can be seen from Fig. 19.

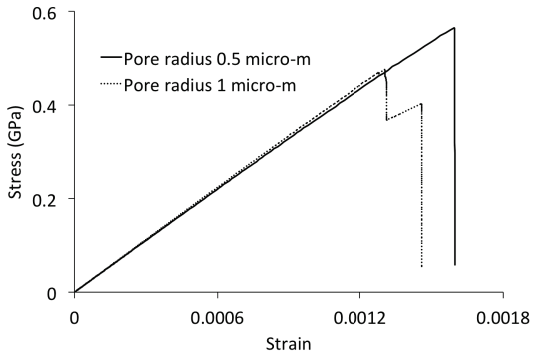

Figure 19: Comparison of stress-strain evolution along the primary loading direction for different pore size but same porosity.

4.4. Effect of grain size

To obtain the grain size effect, a larger representative volume element of size 80 μm x 80 μm with $\sim$32 grains with average grain size of 16 μm is considered. The microstructure for a porosity of 2% and uniform pore diameter of 1 μm is shown in Fig. 20(a). For the same porosity, a larger grain size implies a more porous grain boundary that can cause earlier failure. This is obtained from the phase-field based fracture simulations and is shown in Fig. 21. The failed configuration is shown in Fig. 20(b).

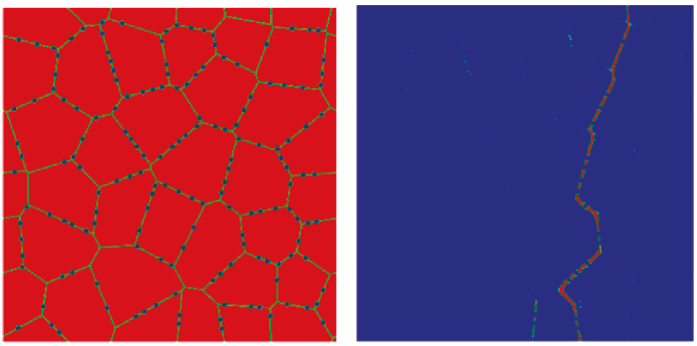

(a) (b)

Figure 20: (a) Representative volume element containing ∼32 grains with average grain size of 16 μm. (b) Final configuration.

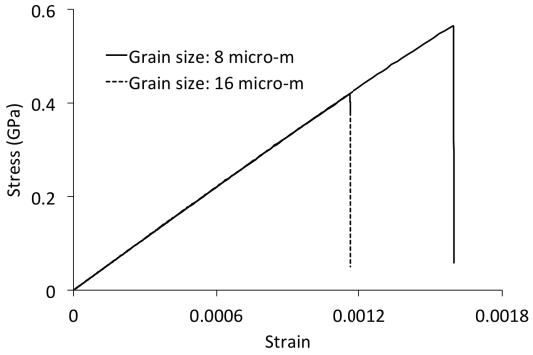

Figure 21: Comparison of stress-strain evolution for different grain sizes.

5. Engineering scale fracture model and associated parameters

The model proposed in [15] is used to describe the brittle fracture behavior at the engineering scale. In this model, the stress in an isotropic material is described by

$$\underline{\sigma} = \underline{\underline{C}} : \underline{\epsilon} \tag{14}$$

where

$$\underline{\underline{C}} = \underline{\underline{C}}(0) - \underline{\underline{E}}(t)\underline{\underline{C}}(0)\underline{\underline{E}}(t) \tag{15}$$

In Eq. 15, $\underline{\sigma}$ and $\underline{\epsilon}$ are the principal stress and strain tensors, respectively, $\underline{\underline{C}}(0)$ is the undamaged stiffness matrix and $\underline{\underline{E}}(\mathrm{t})$ is a diagonal matrix incorporating damage along the 3 orthogonal direction $e_1(\mathrm{t})$, $e_2(\mathrm{t})$ and $e_3(\mathrm{t})$. In this model, damage initiation causes immediate loss of stiffness of the material, which is typical for brittle fracture. Hence, $e_a(\mathrm{t})$, where a=1,2,3 can be represented as

$$e_a(t) = \begin{cases} 0, & \text{for } t < t_1 \\ 1, & \text{otherwise} \end{cases} \tag{16}$$

Presently, only the stress-strain behavior obtained for varying porosities for a fixed pore diameter of 1 μm is fitted to this model. A stress-based criterion is used to define the evolution of e_a as

$$e_a(t) = \begin{cases} 0, & \text{for } \sigma_a(t) < \sigma_f \\ 1, & \text{otherwise} \end{cases} \tag{17}$$

where σ_f is the fracture stress. The stress-strain evolution for porosity of 2% and $\epsilon_2/\epsilon_1 = 0$ is used to fit the model. Subsequently, the effective elastic modulus and fracture stress obtained from the fit is validated by comparing the stress-strain evolution for $\epsilon_2/\epsilon_1 = 1$ and is shown in Fig. 22. As can be observed from the figure, the stress-based model provides a good description of brittle fracture at the engineering scale.

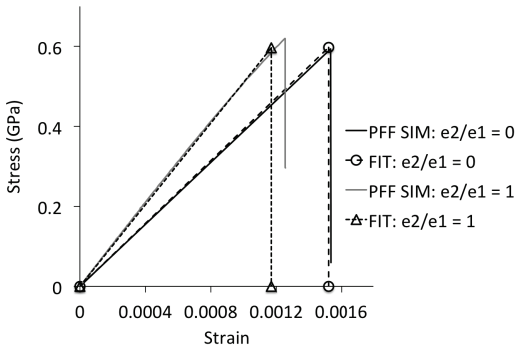

Figure 22: Comparison of stress-strain evolution between the phase-field based fracture simulation and the stress-based model (Eqs. 14 -17).

Analytical equations relating porosity to the effective elastic modulus and fracture stress are obtained by fitting the stress-strain evolution obtained

from the phase-field fracture simulations with the stress-based model. The variations of the effective elastic modulus and fracture stress with porosity are shown in Fig. 23.

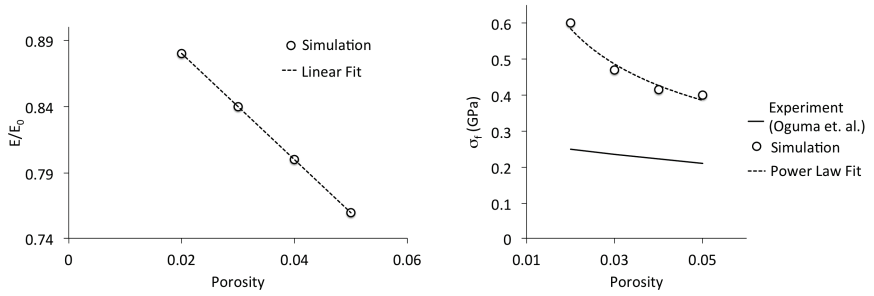

(a) (b)

Figure 23: Variation of: (a) Effective elastic modulus, and (b) Fracture stress with porosity.

A linear fit of the elastic modulus provides $E = E_0(A - Bp)$ where A = 1.0, B=4.0 and p is the porosity. Similar linear relationship with a lower value of B=2.32 has been obtained in [33] using the ultrasonic technique. The variation of fracture stress is fitted with a power-law equation $\sigma_f = \sigma_0 p^{-m}$ where $\sigma_0 = 99.4$ MPa and $m = 0.453$. An exponential functional form obtained from biaxial flexure test has been reported in [6] describing the porosity, average pore and grain size effect on fracture stress. A comparison with the present model by substituting the average grain and pore size of 8 μm and 1 μm, respectively, in their equation is showin in Fig. 23(b). A difference can be observed and can be due to the following:

1. In the simulations only intergranular fracture is considered, though transgranular fracture has been observed in experiments [1].
2. In the simulations only a single grain boundary type has been considered to evaluate the phase-field model parameters. The consideration of other grain boundary types may provide more realistic results.
3. A 2-D approximation of the real microstructure also affects the fracture stress and energy values obtained from the phase-field simulations.

6. Conclusion

In this work, a multi-scale framework using a phase-field based model is developed to investigate the microstructure dependent intergranular brittle

fracture in UO_2. Sensitivity studies have been performed to ensure that the appropriate length scale and viscosity parameters, used in the phase-field model, are chosen to obtain near rate independent sharp crack growth. The energy release rate type parameter used in the phase-field model is then calibrated from molecular dynamics simulation. Subsequently, a numerical sensitivity study is performed whereby the effect of porosity, pore and grain size on the fracture behavior is explored. The response from the micromechanical simulations are then fitted to a stress based model usable at the engineering scale. Presently, predictions are made solely based on brittle intergranular fracture. However, transgranular and ductile fracture can also be incorporated following a similar methodology to obtain improved predictions. The proposed multi-scale approach bridges 3 different scales and allows engineering scale model development using minimal number of experiments.

7. Acknowledgment

This work was funded by the DOE Nuclear Energy Advanced Modeling and Simulation Program.

References

[1] A. G. Evans, R. W. Davidge, The strength and fracture of stoichiometric polycrystalline UO_2, Journal of Nuclear Materials 33 (1969) 249–260.

[2] R. Canon, J. Roberts, R. Beals, Deformation of UO_2 at high temperatures, Journal of the American Ceramic Society 54 (1971) 105–112.

[3] J. T. A. Roberts, Y. Ueda, Influence of porosity on deformation and fracture in UO_2, Journal of the American Ceramic Society 55 (1972) 117–124.

[4] N. Igata, K. Domoto, Fracture stress and elastic modulus of uranium dioxide including excess oxygen, Journal of Nuclear Materials 45 (1972) 317–322.

[5] K. Radford, Effect of fabrication parameters and microstructure on the mechanical strength of fuel pellets, Journal of Nuclear Materials 33 (1979) 222–236.

[6] M. Oguma, Microstructure effects on fracture strength of UO_2 fuel pellets, Journal of Nuclear Science and Technology 19 (1982) 1005–1014.

[7] T. Tachibana, H. Furuya, M. Koizumi, Effect of temperature and deformation rate on fracture strength of sintered uranium dioxide, Journal of Nuclear Science and Technology 16 (1979) 266–277.

[8] H. Matzke, T. Inoue, R. Warren, The surface energy of as determined by hertzian indentation, Journal of Nuclear Materials 91 (1980) 205–220.

[9] T. Kutty, K. Chandrasekharan, J. P. Panakkal, J. Ghosh, Fracture toughness and fracture surface energy of sintered uranium dioxide fuel pellets, Journal of Materials Science Letters 6 (1987) 260–262.

[10] K. Kapoor, A. Ahmad, A. Laksminarayana, G. H. Rao, Fracture properties of sintered UO_2 ceramic pellets with duplex microstructure, Journal of Nuclear Materials 366 (2007) 87–98.

[11] H. Huang, B. Spencer, J. Hales, Discrete element method for simulation of early-life thermal fracturing behavior in ceramic nuclear fuel pellets, Nuclear Engineering and Design 278 (2014) 87–98.

[12] R. Williamson, D. Knoll, Simulating dynamic fracture in oxide fuel pellets using cohesive models, in: 20^{th} International Conference on Structural Mechanics in Reactor Technology, 2009.

[13] J. M. Gatt, J. Sercombe, I. Aubrun, J. Menard, Experimental and numerical study of fracture mechanisms in UO_2 nuclear fuel, Engineering Failure Analysis (2014).

[14] J. Hales, S. Novascone, B. Spencer, R. Williamson, G. Pastore, D. Perez, Verification of the bison fuel performance code, Annals of Nuclear Energy 71 (2014) 81–90.

[15] Y. Rashid, Ultimate strength analysis of prestressed concrete pressure vessels, Nuclear Engineering and Design 7 (1968) 334–344.

[16] Y. Zhang, P. Millett, M. Tonks, X.-M. Bai, S. B. Biner, Molecular dynamics simulations of intergranular fracture in UO_2 with nine empirical interatomic potentials, Journal of Nuclear Materials 452 (2014) 296–303.

[17] C. Miehe, F. Welschinger, M. Hofacker, Thermodynamically consistent phase-field models of fracture: Variational principles and multi-field FE implementations, International Journal for Numerical Methods in Engineering 83 (2010) 1273–1311.

[18] C. Miehe, M. Hofacker, F. Welschinger, A phase field model for rate-independent crack propagation: Robust algorithmic implementation based on operator splits, Computer Methods in Applied Mechanics and Engineering 199 (2010) 2765–2778.

[19] L. Chen, Phase-field models for microstructure evolution, Annual Review of Materials Research 32 (2002) 113–140.

[20] J. Cahn, On spinodal decomposition, Acta Metallurgica 9 (1961) 795–801.

[21] J. W. Cahn, J. E. Hilliard, Free energy of a nonuniform system. I. Interfacial free energy, Journal of Chemical Physics 28 (1958) 258–267.

[22] A. Karma, D. A. Kessler, H. Levine, Phase-field model of mode III dynamic fracture, Physical Review Letters 87 (2001) 045501–1–4.

[23] A. Karma, A. E. Lobkovsky, Unsteady crack motion and branching in a phase-field model of brittle fracture, Physical Review Letters 93 (2004) 245510.

[24] H. Henry, H. Levine, Dynamic instabilities of fracture under biaxial strain using a phase field model, Physical Review Letters 93 (2004) 105504.

[25] R. Spatschek, C. M. Gugenberger, E. Brener, Phase field modeling of fracture and stress-induced phase transitions, Physical Review E 75 (2007) 066111.

[26] H. Amor, J. J. Marigo, C. Maurini, Regularized formulation of the variational brittle fracture with unilateral contact: Numerical experiments, Journal of the Mechanics and Physics of Solids 57 (2009) 1209–1229.

[27] S. Biner, S. Hu, Simulation of damage evolution in composites: A phase-field model, Acta Materialia 57 (2009) 2088–2097.

[28] S. Biner, S. Hu, Simulation of damage evolution in discontinuously reinforced metal matrix composites: a phase-field model, International Journal of Fracture 158 (2009) 99–105.

[29] J. Cho, K. S. Lee, Finite element simulation of crack propagation based on phase field theory, Journal of Mechanical Science and Technology 27 (2013) 3073–3085.

[30] MOOSE: Multiphysics Object Oriented Simulation Environment, Idaho National Lab., USA, URL:http://mooseframework.org/, 2014.

[31] ABAQUS version 6.12, Dassault Systems Simulia Corp., Providence, RI, USA, 2012.

[32] K. Govers, Comparison of interatomic potentials for UO_2, Journal of Nuclear Materials 366 (2007) 161–177.

[33] J. Boocock, A. S. Furzer, J. R. Matthews, The Effect of Porosity on the Elastic Moduli of UO_2 as Measured by an UltraSonic Technique, Report, AERE-M2565, Process Technology Division, Atomic Energy Res. Establishment, Berkshire, England, 1972.